Dendritic compartmentalization of input-specific integration and plasticity rules across cortical development

Courtney E. Yaeger, Dimitra Vardalaki, Norma J. Brown, & Mark T. Harnett[1]

[1]McGovern Institute for Brain Research and Department of Brain and Cognitive Sciences, MIT, Cambridge, MA, USA

To whom correspondence should be addressed: Harnett (harnett@mit.edu)

Summary

Lifelong learning is the ability to continually acquire new information and build upon existing knowledge. Biological and artificial neurons gain and refine internal representations by modifying synaptic weights, but it is unclear how previous knowledge remains stable in spite of ongoing plasticity. Here we show that cortical pyramidal neurons solve this plasticity-stability dilemma by differentially regulating synaptic plasticity within dendritic compartments. We found that oblique dendrites of layer 5 pyramidal neurons in adult mouse primary visual cortex (V1) selectively receive monosynaptic input from dorsal lateral geniculate nucleus (dLGN), integrate linearly, and—surprisingly—lack synaptic potentiation. In contrast, basal dendrites, which do not receive dLGN input, exhibit conventional NMDA receptor (NMDAR)-mediated supralinear integration and synaptic potentiation. Both dendritic compartments initially express NMDAR-mediated supralinear integration and synaptic potentiation during development, but oblique dendritic properties diverge after a critical period of early visual experience. This developmental transition was accompanied by a decrease in relative NMDAR receptor activity and expression at spiny synapses on oblique dendrites. Our results demonstrate a new biological mechanism for how single neurons can safeguard inputs from ongoing experience-dependent plasticity by altering synaptic properties of dendritic domains.

Introduction

The brain learns continuously through a balance of plasticity and stability, where new information is integrated without disrupting prior knowledge. While the plasticity of synaptic weights is fundamental for learning, neural circuits must exhibit sufficient synaptic stability to maintain storage of critical information. This process poses a major unsolved problem for both

biological and artificial neural networks, known as the plasticity-stability dilemma (Ditzler et al., 2015; Grossberg, 1980, 2013; Mermillod et al., 2013; Parisi et al., 2019). In artificial learning systems, this problem manifests as catastrophic forgetting, where previously acquired information is overwritten unless weight changes are limited (Hassabis et al., 2017; McClelland and Rumelhart, 1985; McCloskey and Cohen, 1989). While half a century of experimental and theoretical work on biological synaptic plasticity has focused on how plasticity is induced (Froemke et al., 2005; Golding et al., 2002; Gordon et al., 2006; Kampa et al., 2006; Kumar et al., 2021; Letzkus et al., 2006; Magó et al., 2020; Markram et al., 1997; Sjöström and Häusser, 2006; Weber et al., 2016) and maintained within a working range (Abraham, 2008; Bienenstock et al., 1982; Cooper and Bear, 2012; Lee and Kirkwood, 2019; Li et al., 2019; Turrigiano, 2008), little is currently known about how neurons sustain fundamental information throughout a lifetime of experience-dependent plasticity.

In the mammalian sensory cortex, the first plasticity-stability challenge occurs during early postnatal development. Initial sensory experiences must be stored and stabilized for robust sensory processing, but cortical circuits must maintain flexibility to accommodate subsequent learning. For example, primary sensory inputs in the visual cortex (V1) from the dorsal lateral geniculate nucleus of the thalamus (dLGN) rapidly change at the onset of vision (Faguet et al., 2009; Gu and Cang, 2016; Leighton and Lohmann, 2016; Wiesel and Hubel, 196 3). By adulthood, these inputs are stable and no longer plastic during normal visual experience (Gordon and Stryker, 1996; Rose et al., 2016; Tan et al., 2020; Wang et al., 2010). However, higher-order cortical representations remain highly plastic (Makino and Komiyama, 2015; Pakan et al., 2018; Poort et al., 2015; Weskelblatt and Niell, 2019). Because single cortical neurons receive spatially-targeted inputs (Lafourcade et al., 2022; Morgenstern et al., 2016; Petreanu et al., 2009; Young et al., 2021), we hypothesized that dendritic compartmentalization could arbitrate plasticity or stability for different kinds of information. Using glutamate uncaging, focal stimulation, and super-resolution microscopy, we identified dLGN-recipient and nonrecipient dendritic domains within layer 5 pyramidal neurons (PNs) and tracked the synaptic properties and plasticity of these domains across maturation.

Results

L5 PN oblique dendrites selectively receive thalamic input and exhibit distinct integrative properties from basal dendrites

Visual information from dLGN (Antonini et al., 1999) projects primarily to V1 layer 4 cells. In an analogous sensory cortex, first-order thalamic inputs also synapse on L5 PNs

(Constantinople and Bruno, 2013), which integrate inputs from all cortical layers. Physiological data from juvenile V1 (Morgenstern et al., 2016) and anatomical data (Peters and Feldman, 1977) suggest that dLGN inputs target the apical oblique dendrites of L5 PNs, which can reside in layer 4. To directly test where dLGN inputs make functional synapses on L5 PNs in mouse V1, we employed subcellular channelrhodopsin (ChR2)-assisted circuit mapping (Petreanu et al., 2009). After viral expression of ChR2 in dLGN (Fig 1a), we performed whole-cell patch-clamp recordings from V1 L5 PNs in acute slices from adult mice (P56+). Local photostimulation of ChR2-expressing dLGN boutons across the dendritic tree revealed monosynaptic connections restricted to apical oblique branches (Fig 1b,c).

Given the specific targeting of dLGN inputs to L5 PN oblique dendrites, we asked whether these branches exhibited distinct properties compared to nearby basal dendrites (Fig 1d). In acute slices from adult mice, basal dendrites displayed highly supralinear integration and large local calcium influx in response to spatiotemporally-clustered two-photon glutamate uncaging (Fig 1e,f,g), consistent with previous reports of NMDA spikes in juvenile cortex (Schiller et al., 2000). In contrast, oblique dendrites integrated inputs linearly until axosomatic action potential threshold was reached and did not show significant subthreshold calcium influx (Fig. 1e,f,g). These differences could not be explained by the size of uncaging events, the number of inputs, distance from the soma, action potential threshold, or δV/δt prior to action potential (Supplemental Fig. 1). Thus, in adult V1 L5 PNs, oblique dendrites selectively receive dLGN input and exhibit a specialized linear integration mode.

Oblique dendrites lack synaptic potentiation in adult V1 L5 PNs

Because oblique dendrites did not exhibit large local calcium signals, we hypothesized that synapses on these branches should potentiate less than those on basal dendrites. We tested synaptic potentiation within dendritic compartments by pairing focal electrical stimulation of presynaptic axons at basal or oblique dendrites with somatic current injection. A theta glass bipolar stimulating electrode was positioned within 10 µm of either a basal or an oblique dendritic branch (Fig. 2a,b, Supplemental Fig. 2.) to generate a 1 to 2 mV excitatory postsynaptic potential (EPSP) in the presence of a GABA-A antagonist. EPSPs were paired with 20 ms somatic current injections that drove bursts of 2-4 action potentials. The peak of the EPSP and the peak of the first action potential were within 10 ms of each other, and 5 pairings at 10 Hz were repeated 30 times, with 10 seconds between epochs (Fig. 2c). This protocol strongly potentiated synapses on basal dendrites (Fig. 2d,f, Supplemental Fig. 2), similar to findings in juvenile cortex (Gordon et al., 2006). Potentiation at basal branches required pre-

and postsynaptic coincidence and NMDARs (Supplemental Fig. 2). In contrast, synapses on oblique dendrites did not show any significant potentiation after pairing (Fig. 2e,f, Supplemental Fig. 2). Increasing the numbers of pairings did not change this outcome (Supplemental Fig. 2). These findings indicate that, unlike basal dendrites, oblique branches of L5 PNs in adult V1 lack synaptic potentiation.

Synapses at oblique dendrites are plastic during a postnatal critical period

In V1, dLGN inputs are refined during early postnatal development (Cang et al., 2005; Gu and Cang, 2016; Sommeijer et al., 2017), after which synaptic potentiation at some cortical synapses show a developmental decline (Crair and Malenka, 1995; Kirkwood et al., 1995). Therefore, we hypothesized that synapses on oblique L5 PN dendrites may exhibit NMDAR-mediated supralinear integration and plasticity during early postnatal development. We found that at eye-opening (postnatal days 12-14), oblique and basal dendrites displayed similar NMDAR-dependent supralinearities and large local calcium signals (Fig. 3a-c, Supplemental Fig. 3). These properties persisted into the canonical critical period (P18-22) (Feldman, 2009; Gordon and Stryker, 1996). By 4 weeks of age (P28-P32), oblique dendrites had developed adult-like properties, with linear synaptic integration and minimal local calcium signals (Fig 3c, Supplemental Fig. 3). Synaptic plasticity at oblique dendrites followed the same developmental trajectory: except for P28, when integrative properties were adult-like, oblique and basal dendrites exhibited NMDAR-dependent synaptic potentiation at juvenile ages (Fig. 3d, Supplemental Fig. 3). These findings suggested that visual experience mediates the maturation of oblique dendrite properties; to test this, we conducted these same experiments in mice deprived of light from birth. In P28 dark-reared animals, oblique dendrites retained supralinear integration with large local calcium signals and synaptic potentiation (Fig. 3e, Supplemental Figs. 3). Dark-reared mice re-exposed to a normal light cycle did not develop adult-like integrative properties (Supplemental Fig. 3), indicating that the oblique compartment developed mature properties only during a specific window in development. Collectively, these results demonstrate a restricted developmental window in which visually-driven thalamic activity shifts the L5 PN oblique dendritic compartment towards a linear integration mode with synapses that do not potentiate.

Oblique dendrites develop distinct postsynaptic receptor composition

One possible interpretation of our data is that adult oblique dendrites lack large local calcium signals, integrate linearly, and do not potentiate due to a higher AMPA/NMDA ratio, as

adult cortical AMPA receptors (AMPARs) are significantly less Ca^{2+}-permeable than NMDARs (Hadzic et al., 2017; Kumar et al., 2002). To test this, we compared AMPAR and NMDAR-mediated responses at single spines from basal and oblique dendrites at P21 and in adults. Glutamate uncaging produced AMPAR-mediated EPSPs within the physiological range at single spines, below the threshold for calcium influx (Fig. 4a, Supplemental Fig. 4). Then, Mg^{2+}-free ACSF containing the AMPAR antagonist DNQX was washed in and the uncaging protocol was repeated to assess synaptic NMDARs (Fig. 4b). The average maximum amplitudes of EPSPs under each condition were compared as an AMPA/NMDA ratio. At postnatal day 21, when oblique dendrites behave similarly to basal dendrites, spines from the two branch types had comparable AMPA/NMDA ratios. By adulthood, this ratio increased for oblique dendrites (Fig. 4c), indicating relatively less NMDAR-mediated synaptic conductance, consistent with linear integration, smaller local Ca^{2+} signals, and a decreased capacity for synaptic potentiation.

To provide complementary proteomic evidence for our observed changes in functional AMPA/NMDA, we acquired super-resolution images of oblique and basal dendrites and their synaptic receptor content using epitope-preserving Magnified Analysis of the Proteome (eMAP, Fig. 4d) (Ku et al., 2016; Park et al., 2021). Fixed slices from V1 of adult Thy1-GFP-M mice were expanded to 4x size and stained with antibodies against the presynaptic marker bassoon, the obligate NMDAR subunit GluN1, and GluA1 and GluA2, the predominant AMPAR subunits in cortex (Cheng et al., 2006). Oblique and basal dendrites from L5 PNs were imaged with confocal microscope in ~18 µm-long segments (~75 µm expanded), and dendritic protrusions were annotated (Fig. 4e, f). Immature spines and protrusions without bassoon were excluded post hoc (although basal and oblique branches had similar numbers of immature and mature spines; Supplemental Fig. 4). For each spine head, the intensity of each fluorophore was spatially integrated (Fig. 4g), and the ratio of GluA1+GluA2/NR1 was taken. Oblique dendrite synapses exhibited higher AMPA/NMDA ratios than basal dendrites (Fig. 4h, Supplemental Fig. 4). This effect was pronounced in large spines (Fig. 4i). Taken together, these results indicate that oblique dendrites have relatively less NMDAR content and conductance, and this underlies the differences in integration and plasticity rules between basal and oblique dendritic compartments.

Discussion

Our results reveal that cortical dendrites balance plasticity and stability through experience-dependent regulation of synaptic content within specific dendritic domains. After early visual experience, dLGN-recipient dendrites of L5 PNs lose NMDAR-mediated properties,

creating an entire dendritic domain with linearly-integrating synapses that are unable to potentiate. Our findings align with a recent study in adult association cortex which also observed linearly integrating oblique dendrites (Lafourcade et al., 2022). Together, these findings demonstrate that NMDAR-mediated integration is not universal within the dendritic tree of adult cortical neurons, in contrast to prior theories (Larkum et al. 2009). Here, we find that this dendritic heterogeneity extends to NDMAR-mediated plasticity. While our results do not rule out other possible plasticity mechanisms in oblique dendrites, limited NMDAR-mediated calcium influx constrains their potential to engage conventional molecular cascades (Malenka and Bear 2004).

The decline of NMDAR-mediated properties in thalamorecipient dendrites required early visual experience and could be permanently prevented by delaying the onset of vision. Thus, we discovered that critical periods—the developmental window of experience required for normal connectivity and function—occur at the subcellular level, an unprecedented degree of specificity (Daw, 2009; Feldman, 2009; Hooks and Chen, 2020). Our results indicate that the onset of vision drives strong plasticity within thalamorecipient dendrites until further long-term potentiation cannot be achieved. This limitation of plasticity was accompanied by an increase in AMPA/NMDA ratio and the loss of NMDAR-mediated properties on oblique dendrites. Collectively, our findings establish a tractable new model for future studies on the complete molecular and physiological underpinnings of input-specific synaptic plasticity regulation (Bredt & Nicoll 2003; Malinow & Malenka 2002; Abraham, 2008; Hadzic et al., 2017; Clem et al., 2008; Erisir and Harris, 2003; Lohmann and Kessels, 2014; Kumar et al., 2002; Liu and Cull-Candy, 2000; Monyer et al., 1994; Philpot et al., 2007; Yoshimura et al., 2003).

Protecting knowledge while continually acquiring new information is a long-standing challenge for models of phenomenological plasticity and biologically-inspired neural networks, which are prone to instability and catastrophic forgetting (Hassabis et al., 2017; Parisi et al., 2019). To resolve this plasticity-stability dilemma, some models employ upper limits for synaptic strength or weight changes (Miller and MacKay, 1994; Song et al., 2000). Here we report the first biological evidence for these theoretical limitations: after an initial strengthening in early development, inputs at oblique dendrites are effectively stabilized through a change in synaptic content. This complements other theories and experimental findings that suggest that the capacity for synaptic plasticity depends on current activity and prior plasticity history (Abraham and Bear, 1996; Bear,1995; Fusi et al., 2005; Kirkwood et al., 1996; Lee et al., 2010). However, we find that the limitation of plasticity is a distinct feature of the adult thalamorecipient dendritic domain of L5 PNs. Importantly, synaptic potentiation and NMDAR-mediated properties were

intact in other, non-thalamorecipient dendritic domains of the same cells. Our results likely extend to other cortical neurons, as PNs in all layers of primary sensory cortex receive both first-order thalamic and intracortical inputs (Antonini et al., 1999; Cruz Martín et al., 2014; Harris and Shepherd, 2015; Morgenstern et al., 2016). Thus, cortical neurons may limit plasticity within specific dendrites to maintain essential representations without compromising higher-order input plasticity. The restriction of plasticity within select dendritic compartments is a powerful mechanism by which single neurons can solve the tradeoff between flexibility and stability inherent to all learning systems.

Acknowledgements

We thank Mark Bear, Elly Nedivi, Josh Trachtenberg, and the Harnett laboratory for their comments and suggestions and Kwanghun Chung for generously sharing equipment. This work was funded by a Life Sciences Research Foundation postdoctoral fellowship (C.E.Y.), and a Vallee Foundation Scholars Award, the James W. and Patricia T. Poitras Fund, and the National Institutes of Health R01NS106031 (M.T.H.).

Author Contributions

C.E.Y. and M.T.H. conceived of the experiments. C.E.Y. carried out all physiology experiments and analyses. D.V. conducted the eMAP experiments and C.E.Y. analyzed the data. N.J.B. performed viral injections and histology. M.T.H. supervised all aspects of the project and wrote the manuscript with C.E.Y.

Declaration of interests

Authors declare that they have no competing interests.

Methods

Animals

All animal procedures were carried out in accordance with NIH and Massachusetts Institute of Technology Committee on Animal Care guidelines. C57BL6 male and female mice (Charles River Laboratories) were used in approximately equal numbers. Mice 8 weeks and older (P56+) were used for adult mouse experiments. For developmental timepoints, mice ages P10-P14, P18-22, and P28-P32 were used. All animals were kept in conventional social housing with unlimited food and water on a 12-hour light/dark cycle. For dark-rearing experiments, pregnant dams were moved to a dark room at E18 and pups were born and raised in complete darkness,

with red light exposure during cage changes. Dark reared mice were ages P28-P32 at the time of experimentation. 8-week-old Thy-1-GFP-M mice (Jackson Laboratory) were used for eMAP experiments.

Slice preparation

Sucrose-containing artificial cerebrospinal fluid (sACSF) was used during the slicing procedure, containing (in mM): 90 sucrose, 60 sodium chloride, 26.5 sodium bicarbonate, 2.75 potassium chloride, 1.25 sodium phosphate, 9 glucose, 1.1 calcium chloride, and 4.1 magnesium chloride, with an osmolality of 295-302. The sucrose solution was partially frozen to create a small amount of slush and was kept ice-cold. Artificial cerebrospinal fluid (ACSF) was used for recovery and recording, containing (in mM): 122 sodium chloride, 25 sodium bicarbonate, 3 potassium chloride, 1.25 sodium phosphate, 12 glucose, 1.2 calcium chloride, 1.2 magnesium chloride, 1 ascorbate, and 3 sodium pyruvate, with an osmolality of 302-307. All solutions were saturated with carbogen, 5% CO_2 and 95% O_2. Acute slice preparation was consistent for all ages and experiments. Mice were put under isoflurane-induced anesthesia and decapitated. The brain was extracted in ice-cold sucrose solution in less than one minute. The brain was blocked at a moderate angle (approximately 20 degrees from coronal) to favor the preservation of apical dendrites in the occipital cortex. After the brain was mounted and submerged in ice-cold sACSF, a vibratome (Lieca VT1200S) was used to cut 300 µm-thick slices, which were transferred to ACSF for 30-50 minutes at 36°C. Longer recovery times were used for tissue collected from younger animals. Following recovery, slices were kept at room temperature.

Patch-clamp recording

Recordings were performed in ACSF (concentrations noted above) at 34–36 °C. Intracellular recording solution contained (in mM): 134 potassium gluconate, 6 KCl, 10 HEPES, 4 NaCl, 4 Mg_2ATP, 0.3 NaGTP, and 14 phosphocreatine di(tris). Depending on the experiment, 0.05 mM Alexa 594, 0.1 mM Alexa 488, and/or 0.1 mM OGB-1 (Invitrogen) were added to the internal solution. Whole-cell current-clamp recordings were obtained with a Dagan BVC-700A amplifier. Patch pipettes with thin-wall glass (1.5/1.0mm OD/ID, WPI) and resistances of 3-7 MΩ were used. Pipette capacitance was fully neutralized prior to break-in, and series resistance was kept fully balanced throughout, ranging from 5-30 MΩ. The liquid junction potential was not corrected. Current signals were digitized at 20 kHz and filtered at 10 kHz (Prairie View). L5 PNs were characterized by their large somas in layer 5, thick apical dendrites, broad arborization in layer 1, low input resistance, and prominent voltage sag.

Virus injection

For sCRACM experiments, AAV2-hSyn-hChR2(H134R)-mCherry (UNC Vector Core) was expressed in neurons in the dorsal lateral geniculate nucleus. Mice 6 weeks or older were injected 4 weeks or more before slice preparation. Under isoflurane anesthesia, mice were secured on a stereotaxic apparatus with a feedback-controlled heating pad (DC Temperature Control System, FHC). Slow-release buprenorphine (1 mg/kg) was administered subcutaneously. After scalp incision, a small burr hole was drilled over the injection site at the following coordinates relative to bregma: anterior-posterior 2.7-2.8 mm; medio-lateral 2.3-2.4 mm. A beveled microinjection pipette containing was lowered to a depth of 2.7-2.9 mm, and approximately 100 nL of virus was injected at a rate of 50 nL/min using a Nanoject. Following virus injection and a five-minute rest, the pipette was removed and the incision was sutured. Accuracy of the injection was assessed in acute slices using two-photon microscopy. For image clarity, histology in Figure 1 was taken from a brain that was perfused, stored at 4°C overnight in 4% paraformaldehyde, transferred to PBS, and sectioned in 100 µm-thick slices. Sections were mounted, coverslipped, and imaged under a confocal microscope (Zeiss LSM 710 with a 10x objective, NA 0.45).

sCRACM

After 4 weeks or more of ChR2 expression in dLGN, acute slices of V1 were prepared. A two-photon laser scanning system (Bruker), with dual galvanometers and a MaiTai DeepSee laser, was used to confirm the presence of mCherry-expressing cell bodies in the dLGN. For all recordings, TTX (1 µM) and 4-AP (100 µM) were added to ACSF to isolate monosynaptic connections. Following whole-cell configuration, a 5 ms 473 nm full-field LED was used to determine if the neuron received inputs from axons containing ChR2. If the LED drove EPSPs or spikes, a 9 by 17 (400 x 800 µm) stimulation grid with 50 µm spacing was positioned over the area containing the entire neuron, aligned at the pia using two-photon imaging under low magnification (4x, 0.16 NA air objective, Olympus) and Prairie View software. The stimulation grid controlled the location of a 473 nm laser beam (OptoEngine, LLC), and the duration of the light pulses was kept to 1-3 ms under <2 mW power. Each point on the grid was stimulated in order, progressing forward by column, with an interpoint delay of 1 s. 3-6 rounds of stimulation were averaged for each neuron. Baseline voltage was defined as the 50 ms before stimulation, and EPSP amplitudes were calculated as the baseline-subtracted maximum voltage within 50 ms after photostimulation. Population data was obtained by rotating the maps to align to the pia,

overlaying the maps to align at the soma, normalizing peak voltages, and averaging across experiments.

Glutamate uncaging

Following whole-cell dialysis with a structural dye via the patch pipette, basal or apical oblique branches were localized using two-photon imaging. A pipette containing caged glutamate (4-methoxy-7-nitroindolinyl-caged-L-glutamate or MNI-glutamate) diluted in ACSF (10 mM) was positioned just above the slice and over the recording site, and a picrospritzer (Picospritzer III, Parker Hannifin) was used to puff a constant flow of caged glutamate into the region of interest. A second Mai-Tai DeepSee laser controlled by Prairie View software was used for photostimulation of MNI-glutamate at 720 nm. Uncaging was targeted just adjacent to spine heads. In the imaging pathway, a linescan was used for simultaneous calcium imaging. Laser intensity for both lasers was independently controlled (Conoptics). Linescan imaging was performed at 1300 Hz, with a dwell time of 8 µs and a total scan time of less than 250 ms, with baseline fluorescence kept minimal and monitored throughout. Cells with signs of photodamage were excluded. The uncaging laser was calibrated to either a threshold calcium signal (~100% ΔF/F) or an action potential, where the minimum power needed to drive either event was identified and used for all points. The uncaging dwell time was 0.2 ms, and the uncaging interval between multiple spines was 0.32 ms. Groups of 2-5 spines were stimulated independently and then in combination with other groups up to a total of 25-40 spines. Expected values were calculated by summing the average response of each group of spines. Ca^{2+} signals are expressed as $(F - F_{baseline})/F_{baseline})$. For acute blockade of NMDA receptors, the competitive antagonist D-AP5 (50 µM) was used.

Spike-timing dependent plasticity

For local branch stimulation, theta glass (2.0/1.4mm OD/ID) housing a bipolar stimulating electrode (ISO-Flex, AMPI) was positioned within 10 µm of a basal or apical oblique branch. Stimulation intensity was calibrated to generate a small EPSP of 1-3 mV, typically requiring 5-20 µA of current from the stimulating electrode. Ten minutes of baseline stimulation at 0.1 Hz was recorded to ensure stability of the EPSP. A -50 pA hyperpolarizing step was included to estimate input resistance. For plasticity induction, EPSPs were paired with a somatic current injection of 400-700 pA for 20 ms duration to produce a train of 2-4 action potentials. The peak of the first action potential was timed to be within 10 ms of the peak of the EPSP. Pairs were done in sets of 5 at 10 Hz, and sets of 5 were repeated 30 times at 0.1 Hz. After the induction

period, EPSPs were monitored for at least 20 minutes. Inclusion criteria were as follows: resting membrane potential could fluctuate from baseline by no more than 3 mV, input resistance could not increase more than 20% of baseline; and series resistance had to be compensated fully throughout (<30 MΩ). Recordings were tested for baseline stability post-hoc using either correlation or linear regression (data not shown), and cells with significant changes in baseline recording were not included. The necessity of pre-post pairing was shown using the same recording set up but driving either the synaptic stimulation or the post-synaptic burst (and not both) during the induction period. For acute blockade of NMDARs, the competitive antagonist D-AP5 (50 µM) was used. Throughout plasticity experiments, picrotoxin (100 µM) was present in the bath to block GABAergic transmission in acute slices from adult mice and at P28. 10 µM picrotoxin was used for acute slices at P21, and no picrotoxin was needed at P14.

Epitope-preserving Magnified Analysis of the Proteome

Mice were perfused with cold PBS followed by cold 4% PFA while under deep anesthesia (5% isoflurane). Brains were removed and kept in the same fixative overnight at 4°C and then washed with PBS at 4°C for at least 1 day. 1.0 mm coronal slices of primary visual cortex were cut on a vibratome and kept in PBS at 4°C until the day of processing. Slices were then incubated eMAP hydrogel monomer solution (30% acrylamide [A9099, MilliporeSigma, St. Louis, MO, USA], 10% sodium acrylate [408220, MilliporeSigma], 0.1% bis-acrylamide [161-0142, Bio-Rad Laboratories, Hercules, CA, USA], and 0.03% VA-044 (w/v) [Wako Chemicals, Richmond, VA, USA] in PBS]), protected from light, at 4°C overnight. For gelation, slices were mounted between glass slides in eMAP solution and sealed in a 50 mL conical tube with nitrogen gas at positive pressure of 10-12 psi at 37°C for 3 hours. The excess gel around the slices was then removed. To reach a first expansion stage of 1.7x, the slices were incubated overnight in a solution of 0.02% sodium azide (w/v) in PBS at 37°C. Slices were trimmed to contain only parts of primary visual cortex and further sectioned with a vibratome to 75 µm thickness (corresponding to ~40 µm thickness of the pre-expanded tissue). Slices containing good candidate cells – layer 5 pyramidal neurons whose apical trunk could be reconstructed at its full length in a single slice or at most two consecutive slices – were selected during live low-resolution confocal imaging sessions. These slices were trimmed to smallest possible samples of approximately 1.0 mm in both width and length. Slices were incubated in tissue clearing solution (6% SDS (w/v), 0.1 M phosphate buffer, 50 mM sodium sulfite, 0.02% sodium azide (w/v), pH 7.4) at 37°C for 6 hours, followed by incubation in preheated clearing solution at 95°C for 10 min. Cleared samples were thoroughly washed with PBS + 0.1% Triton X at 37 °C.

Primary antibody staining was performed at 37°C overnight with the following antibodies: Anti-GFP (Life Technologies A10262), Anti-NMDAR1 (SYSY 114011), Anti-AMPAR1 (SYSY 182003), Anti-AMPAR2 (SYSY 182103), and Anti-Bassoon (SYSY 141004). For secondary staining, the following fluorescent antibodies were used: Bassoon: anti-Guinea pig-405 (AbCam ab175678); GFP: anti-Chicken-488 (Invitrogen A11039); NMDAR1: anti-Mouse-AF+555 (Invitrogen A32727); and AMPAR1 and AMPAR2: anti-Rabbit-AF+647 (Invitrogen A32733). Final expansion was performed just before imaging by putting the trimmed slices in 0.1 mM tris in distilled water, and approximately 4X total linear expansion was achieved. Slices were imaged using Leica TCS SP8 upright confocal DM6000 microscope equipped with a 63x HC PL APO CS2/1.2 W objective, hybrid detectors, and a white light laser. Within slices, intact L5b neurons were identified by their thick trunks and broad apical tufts. Within single neurons, both basal and oblique dendritic branches were imaged. To avoid photobleaching effects, no slice was imaged more than once, and basal and oblique dendrites were imaged in alternating order for each cell. Dendritic protrusions were analyzed using Fiji software. To draw regions of interest within spine heads in the GFP channel, a custom-written macro code was used to apply a median blur (2 pixels), threshold the image, and draw an ROI on the annotated protrusion. Using custom-written code in MATLAB, all color channels were thresholded to include only signals 2 S.D. above the mean fluorescence intensity, and signals from each channel were extracted from the ROI. The plane with peak antibody fluorescence was identified within the spine head ROI, and each channel's fluorescence signals within the plane were summed. Long, thin dendritic protrusions without enlarged heads were classified as filopodia (head diameter/neck diameter < 1.3) and excluded from the final analysis, as were spines with no detectable bassoon.

Data availability

All data and custom-written analysis code are available upon request.

References

Abraham, W.C. (2008). Metaplasticity: tuning synapses and networks for plasticity. Nat. Rev. Neurosci. *9*, 387.

Abraham, W.C., and Bear, M.F. (1996). Metaplasticity: the plasticity of synaptic plasticity. Trends Neurosci. *19*, 126–130.

Antonini, A., Fagiolini, M., and Stryker, M.P. (1999). Anatomical correlates of functional plasticity in mouse visual cortex. J. Neurosci. *19*, 4388–4406.

Bear, M.F. (1995). Mechanism for a sliding synaptic modification threshold. Neuron *15*, 1–4.

Bienenstock, E.L., Cooper, L.N., and Munro, P.W. (1982). Theory for the development of neuron selectivity: orientation specificity and binocular interaction in visual cortex. J. Neurosci. *2*, 32–48.

Bi, G.Q., and Poo, M.M. (1998). Synaptic modifications in cultured hippocampal neurons: dependence on spike timing, synaptic strength, and postsynaptic cell type. J. Neurosci. *18*, 10464–10472.

Bredt DS, Nicoll RA. 2003. AMPA receptor trafficking at excitatory synapses. Neuron. 40(2):361–79

Cang, J., Rentería, R.C., Kaneko, M., Liu, X., Copenhagen, D.R., and Stryker, M.P. (2005). Development of precise maps in visual cortex requires patterned spontaneous activity in the retina. Neuron *48*, 797–809.

Cheng, D., Hoogenraad, C.C., Rush, J., Ramm, E., Schlager, M.A., Duong, D.M., Xu, P., Wijayawardana, S.R., Hanfelt, J., Nakagawa, T., et al. (2006). Relative and absolute quantification of postsynaptic density proteome isolated from rat forebrain and cerebellum. Mol. Cell. Proteomics *5*, 1158–1170.

Clem, R.L., Celikel, T., and Barth, A.L. (2008). Ongoing in vivo experience triggers synaptic metaplasticity in the neocortex. Science *319*, 101–104.

Constantinople, C.M., and Bruno, R.M. (2013). Deep cortical layers are activated directly by thalamus. Science *340*, 1591–1594.

Cooper, L.N., and Bear, M.F. (2012). The BCM theory of synapse modification at 30: interaction of theory with experiment. Nat. Rev. Neurosci. *13*, 798–810.

Crair, M.C., and Malenka, R.C. (1995). A critical period for long-term potentiation at thalamocortical synapses. Nature *375*, 325–328.

Cruz-Martín, A., El-Danaf, R.N., Osakada, F., Sriram, B., Dhande, O.S., Nguyen, P.L., Callaway, E.M., Ghosh, A., and Huberman, A.D. (2014). A dedicated circuit links direction-selective retinal ganglion cells to the primary visual cortex. Nature *507*, 358–361.

Daw, N.W. (2009). The foundations of development and deprivation in the visual system. J Physiol (Lond) *587*, 2769–2773.

Ditzler, G., Roveri, M., Alippi, C., and Polikar, R. (2015). Learning in nonstationary environments: A survey. IEEE Comput. Intell. Mag. *10*, 12–25.

Ehrlich, I., and Malinow, R. (2004). Postsynaptic density 95 controls AMPA receptor incorporation during long-term potentiation and experience-driven synaptic plasticity. J. Neurosci. *24*, 916–927.

Erisir, A., and Harris, J.L. (2003). Decline of the critical period of visual plasticity is concurrent with the reduction of NR2B subunit of the synaptic NMDA receptor in layer 4. J. Neurosci. *23*, 5208–5218.

Faguet, J., Maranhao, B., Smith, S.L., and Trachtenberg, J.T. (2009). Ipsilateral eye cortical maps are uniquely sensitive to binocular plasticity. J. Neurophysiol. *101*, 855–861.

Feldman, D.E. (2009). Synaptic mechanisms for plasticity in neocortex. Annu. Rev. Neurosci. *32*, 33–55.

Froemke, R.C., Poo, M.-M., and Dan, Y. (2005). Spike-timing-dependent synaptic plasticity depends on dendritic location. Nature *434*, 221–225.

Fusi, S., Drew, P.J., and Abbott, L.F. (2005). Cascade models of synaptically stored memories. Neuron *45*, 599–611.

Golding, N.L., Staff, N.P., and Spruston, N. (2002). Dendritic spikes as a mechanism for cooperative long-term potentiation. Nature *418*, 326–331.

Gordon, J.A., and Stryker, M.P. (1996). Experience-dependent plasticity of binocular responses in the primary visual cortex of the mouse. J. Neurosci. *16*, 3274–3286.

Gordon, U., Polsky, A., and Schiller, J. (2006). Plasticity compartments in basal dendrites of neocortical pyramidal neurons. J. Neurosci. *26*, 12717–12726.

Grossberg, S. (1980). How does a brain build a cognitive code? Psychol. Rev. *87*, 1–51.

Grossberg, S. (2013). Adaptive Resonance Theory: how a brain learns to consciously attend, learn, and recognize a changing world. Neural Netw. *37*, 1–47.

Gu, Y., and Cang, J. (2016). Binocular matching of thalamocortical and intracortical circuits in the mouse visual cortex. ELife *5*.

Hadzic, M., Jack, A., and Wahle, P. (2017). Ionotropic glutamate receptors: Which ones, when, and where in the mammalian neocortex. J. Comp. Neurol. *525*, 976–1033.

Harris, K.D., and Shepherd, G.M.G. (2015). The neocortical circuit: themes and variations. Nat. Neurosci. *18*, 170–181.

Hassabis, D., Kumaran, D., Summerfield, C., and Botvinick, M. (2017). Neuroscience-Inspired Artificial Intelligence. Neuron *95*, 245–258.

Hooks, B.M., and Chen, C. (2020). Circuitry Underlying Experience-Dependent Plasticity in the Mouse Visual System. Neuron *106*, 21–36.

Kampa, B.M., Letzkus, J.J., and Stuart, G.J. (2006). Requirement of dendritic calcium spikes for induction of spike-timing-dependent synaptic plasticity. J Physiol (Lond) *574*, 283–290.

Kirkwood, A., Lee, H.K., and Bear, M.F. (1995). Co-regulation of long-term potentiation and experience-dependent synaptic plasticity in visual cortex by age and experience. Nature *375*, 328–331.

Kirkwood, A., Rioult, M.C., and Bear, M.F. (1996). Experience-dependent modification of synaptic plasticity in visual cortex. Nature *381*, 526–528.

Kumar, A., Barkai, E., and Schiller, J. (2021). Plasticity of olfactory bulb inputs mediated by dendritic NMDA-spikes in rodent piriform cortex. ELife *10*.

Kumar, S.S., Bacci, A., Kharazia, V., and Huguenard, J.R. (2002). A developmental switch of AMPA receptor subunits in neocortical pyramidal neurons. J. Neurosci. *22*, 3005–3015.

Ku, T., Swaney, J., Park, J.-Y., Albanese, A., Murray, E., Cho, J.H., Park, Y.-G., Mangena, V., Chen, J., and Chung, K. (2016). Multiplexed and scalable super-resolution imaging of three-dimensional protein localization in size-adjustable tissues. Nat. Biotechnol. *34*, 973–981.

Lafourcade, M., van der Goes, M.-S.H., Vardalaki, D., Brown, N.J., Voigts, J., Yun, D.H., Kim, M.E., Ku, T., and Harnett, M.T. (2022). Differential dendritic integration of long-range inputs in association cortex via subcellular changes in synaptic AMPA-to-NMDA receptor ratio. Neuron.

Larkum, M.E., Nevian, T., Sandler, M., Polsky, A., and Schiller, J. (2009). Synaptic integration in tuft dendrites of layer 5 pyramidal neurons: a new unifying principle. Science *325*, 756–760.

Lee, H.-K., and Kirkwood, A. (2019). Mechanisms of Homeostatic Synaptic Plasticity in vivo. Front. Cell. Neurosci. *13*, 520.

Lee, M.-C., Yasuda, R., and Ehlers, M.D. (2010). Metaplasticity at single glutamatergic synapses. Neuron *66*, 859–870.

Leighton, A.H., and Lohmann, C. (2016). The Wiring of Developing Sensory Circuits-From Patterned Spontaneous Activity to Synaptic Plasticity Mechanisms. Front. Neural Circuits *10*, 71.

Letzkus, J.J., Kampa, B.M., and Stuart, G.J. (2006). Learning rules for spike timing-dependent plasticity depend on dendritic synapse location. J. Neurosci. *26*, 10420–10429.

Liu, S.Q., and Cull-Candy, S.G. (2000). Synaptic activity at calcium-permeable AMPA receptors induces a switch in receptor subtype. Nature *405*, 454–458.

Li, J., Park, E., Zhong, L.R., and Chen, L. (2019). Homeostatic synaptic plasticity as a metaplasticity mechanism - a molecular and cellular perspective. Curr. Opin. Neurobiol. *54*, 44–53.

Lohmann, C., and Kessels, H.W. (2014). The developmental stages of synaptic plasticity. J Physiol (Lond) *592*, 13–31.

Magó, Á., Weber, J.P., Ujfalussy, B.B., and Makara, J.K. (2020). Synaptic Plasticity Depends on the Fine-Scale Input Pattern in Thin Dendrites of CA1 Pyramidal Neurons. J. Neurosci. *40*, 2593–2605.

Makino, H., and Komiyama, T. (2015). Learning enhances the relative impact of top-down processing in the visual cortex. Nat. Neurosci. *18*, 1116–1122.

Malenka, R.C., and Bear, M.F. (2004). LTP and LTD: an embarrassment of riches. Neuron 44, 5–21.

Malinow R, Malenka RC. 2002. AMPA receptor trafficking and synaptic plasticity. Annu. Rev. Neurosci. 25:103–26

Markram, H., Lübke, J., Frotscher, M., and Sakmann, B. (1997). Regulation of synaptic efficacy by coincidence of postsynaptic APs and EPSPs. Science *275*, 213–215.

McClelland, J.L., and Rumelhart, D.E. (1985). Distributed memory and the representation of general and specific information. J. Exp. Psychol. Gen. *114*, 159–197.

McCloskey, M., and Cohen, N.J. (1989). Catastrophic Interference in Connectionist Networks: The Sequential Learning Problem. In Psychology of Learning and Motivation, (Elsevier), pp. 109–165.

Mermillod, M., Bugaiska, A., and Bonin, P. (2013). The stability-plasticity dilemma: investigating the continuum from catastrophic forgetting to age-limited learning effects. Front. Psychol. *4*, 504.

Miller, K.D., and MacKay, D.J.C. (1994). The Role of Constraints in Hebbian Learning. Neural Comput. *6*, 100–126.

Monyer, H., Burnashev, N., Laurie, D.J., Sakmann, B., and Seeburg, P.H. (1994). Developmental and regional expression in the rat brain and functional properties of four NMDA receptors. Neuron *12*, 529–540.

Morgenstern, N.A., Bourg, J., and Petreanu, L. (2016). Multilaminar networks of cortical neurons integrate common inputs from sensory thalamus. Nat. Neurosci. *19*, 1034–1040.

Nakagawa, T., Futai, K., Lashuel, H.A., Lo, I., Okamoto, K., Walz, T., Hayashi, Y., and Sheng, M. (2004). Quaternary structure, protein dynamics, and synaptic function of SAP97 controlled by L27 domain interactions. Neuron *44*, 453–467.

Pakan, J.M.P., Currie, S.P., Fischer, L., and Rochefort, N.L. (2018). The impact of visual cues, reward, and motor feedback on the representation of behaviorally relevant spatial locations in primary visual cortex. Cell Rep. *24*, 2521–2528.

Parisi, G.I., Kemker, R., Part, J.L., Kanan, C., and Wermter, S. (2019). Continual lifelong learning with neural networks: A review. Neural Netw. *113*, 54–71.

Park, J., Khan, S., Yun, D.H., Ku, T., Villa, K.L., Lee, J.E., Zhang, Q., Park, J., Feng, G., Nedivi, E., et al. (2021). Epitope-preserving magnified analysis of proteome (eMAP). Sci. Adv. *7*, eabf6589.

Peters, A., and Feldman, M.L. (1977). The projection of the lateral geniculate nucleus to area 17 of the rat cerebral cortex. IV. Terminations upon spiny dendrites. J. Neurocytol. *6*, 669–689.

Petreanu, L., Mao, T., Sternson, S.M., and Svoboda, K. (2009). The subcellular organization of neocortical excitatory connections. Nature *457*, 1142–1145.

Philpot, B.D., Cho, K.K.A., and Bear, M.F. (2007). Obligatory role of NR2A for metaplasticity in visual cortex. Neuron *53*, 495–502.

Poort, J., Khan, A.G., Pachitariu, M., Nemri, A., Orsolic, I., Krupic, J., Bauza, M., Sahani, M., Keller, G.B., Mrsic-Flogel, T.D., et al. (2015). Learning Enhances Sensory and Multiple Non-sensory Representations in Primary Visual Cortex. Neuron *86*, 1478–1490.

Rose, T., Jaepel, J., Hübener, M., and Bonhoeffer, T. (2016). Cell-specific restoration of stimulus preference after monocular deprivation in the visual cortex. Science *352*, 1319–1322.

van Rossum, M.C., Bi, G.Q., and Turrigiano, G.G. (2000). Stable Hebbian learning from spike timing-dependent plasticity. J. Neurosci. *20*, 8812–8821.

Schiller, J., Major, G., Koester, H.J., and Schiller, Y. (2000). NMDA spikes in basal dendrites of cortical pyramidal neurons. Nature *404*, 285–289.

Sjöström, P.J., and Häusser, M. (2006). A cooperative switch determines the sign of synaptic plasticity in distal dendrites of neocortical pyramidal neurons. Neuron *51*, 227–238.

Sommeijer, J.-P., Ahmadlou, M., Saiepour, M.H., Seignette, K., Min, R., Heimel, J.A., and Levelt, C.N. (2017). Thalamic inhibition regulates critical-period plasticity in visual cortex and thalamus. Nat. Neurosci. *20*, 1715–1721.

Song, S., Miller, K.D., and Abbott, L.F. (2000). Competitive Hebbian learning through spike-timing-dependent synaptic plasticity. Nat. Neurosci. *3*, 919–926.

Stein, V., House, D.R.C., Bredt, D.S., and Nicoll, R.A. (2003). Postsynaptic density-95 mimics and occludes hippocampal long-term potentiation and enhances long-term depression. J. Neurosci. *23*, 5503–5506.

Tan, L., Tring, E., Ringach, D.L., Zipursky, S.L., and Trachtenberg, J.T. (2020). Vision reconstructs the cellular composition of binocular circuitry during the critical period. BioRxiv.

Turrigiano, G.G. (2008). The self-tuning neuron: synaptic scaling of excitatory synapses. Cell *135*, 422–435.

Wang, B.-S., Sarnaik, R., and Cang, J. (2010). Critical period plasticity matches binocular orientation preference in the visual cortex. Neuron *65*, 246–256.

Weber, J.P., Andrásfalvy, B.K., Polito, M., Magó, Á., Ujfalussy, B.B., and Makara, J.K. (2016). Location-dependent synaptic plasticity rules by dendritic spine cooperativity. Nat. Commun. *7*, 11380.

Weskelblatt, J.B., and Niell, C.M. (2019). Distinct functional classes of excitatory neurons in mouse V1 are differentially modulated by learning and task engagement. BioRxiv.

Wiesel, T.N., and Hubel, D.H. (1963). Single-cell responses in striate cortex of kittens deprived of vision in one eye. J. Neurophysiol. *26*, 1003–1017.

Yoshimura, Y., Ohmura, T., and Komatsu, Y. (2003). Two forms of synaptic plasticity with distinct dependence on age, experience, and NMDA receptor subtype in rat visual cortex. J. Neurosci. *23*, 6557–6566.

Young, H., Belbut, B., Baeta, M., and Petreanu, L. (2021). Laminar-specific cortico-cortical loops in mouse visual cortex. ELife *10*.

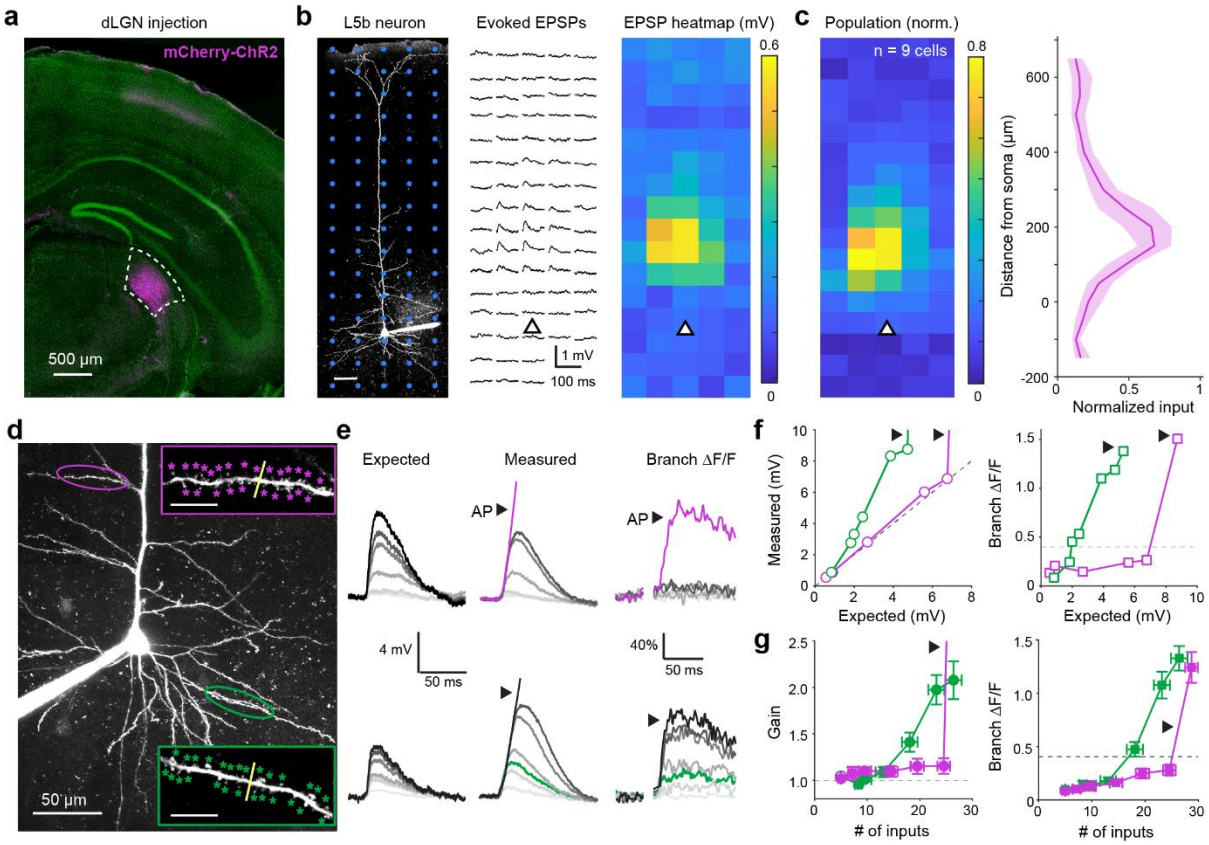

Figure 1: Apical oblique dendrites in L5 PNs of adult V1 are selectively targeted by dLGN inputs and exhibit distinct integrative properties compared to basal dendrites.

a. Example confocal image of a coronal brain slice showing dLGN neurons infected with AAV2-hSyn-mCherry-ChR2.
b. Left: Example two-photon image of a V1 L5 PN whole-cell recording with overlaid photostimulation grid (blue). Scale bar, 50 µm. Middle: Average evoked EPSPs from 6 repetitions of 473 nm photostimulation for the neuron and grid shown. Soma position is indicated by the triangle. Right: Heatmap of average evoked EPSPs. Each square is 50 µm.
c. Left: Normalized heatmap of pooled L5 PNs (n = 9 neurons, 9 slices, 3 P56+ animals), aligned at the soma. Each square is 50 µm. Right: Mean normalized input as a function of depth for all neurons. Shaded region indicates the bootstrapped 95% confidence interval.
d. Example two-photon z-stack of a L5 PN with glutamate uncaging sites indicated on an oblique (purple) and a basal (green) branch. Uncaging sites (stars) and linescan (yellow) are magnified in insets (scale bars: 10 µm).
e. Expected EPSPs, measured EPSPs, and local branch Ca^{2+} signals for oblique (top) and basal (bottom) dendrites shown in d. Left: Expected voltages from linearly summed inputs. Middle: Measured EPSPs in response to increasing numbers of synchronous uncaging inputs. Stimulation of all inputs led to an action potential (AP, arrow). Right: Corresponding change in OGB-1 signal (ΔF/F) with input summation.
f. Measured voltage (left) and branch ΔF/F (right) as a function of expected voltage for the branches shown in d. Dashed line indicates linearity (left) and threshold Ca^{2+} signal (right).
g. Adult population gain (measured/expected, left) and branch ΔF/F (right). n = 13 basal branches from 7 animals and 9 oblique branches from 6 animals. All animals were P56+. Basal AP removed for clarity. Basal vs oblique gain (AP excluded), Mann-Whitney U test: p = 7.63E-04; basal vs oblique ΔF/F (AP excluded), Mann-Whitney U test: p = 1.08E-05.

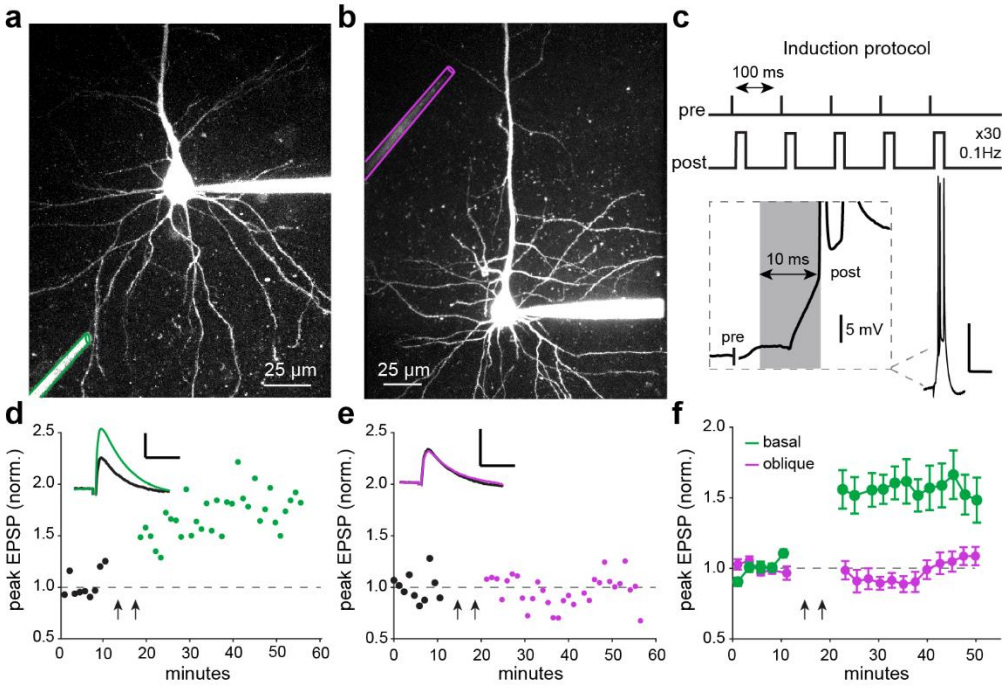

Figure 2: Oblique dendrites in adult V1 L5 PNs lack long-term synaptic potentiation, unlike basal dendrites.

a. Example two-photon z-stack of whole-cell recording with focal stimulation (green) near a basal dendrite.
b. As in a, but for an oblique dendrite (purple).
c. Plasticity induction protocol. 5 pairings of pre- and post-synaptic stimulation at 100 Hz, repeated 30 times at 0.1 Hz. Example trace below, right; inset shows the 10 ms interval between the peak of the evoked EPSP and the peak of the first action potential. Scale bar: 20 mV, 50 ms; inset: 5 mV, 5 ms.
d. Example recording from the basal dendrite shown in a. After 10 minutes of baseline recording, the induction protocol is delivered (arrows denote start and stop). Inset shows average EPSP before (black) and after (color) pairing. Scale bar: 1 mV, 25 ms. Responses are 1 min binned averages.
e. As in d, for the oblique dendrite shown in b.
f. Mean normalized peak EPSP amplitude for neurons stimulated at basal (green) or oblique (purple) branches (2 min bins; n = 10 basal branches from 10 animals and 13 oblique branches from 12 animals. All animals were P56+.). Error bars are s.e.m. Basal vs. oblique post-induction EPSP, Mann-Whitney U test: p = 4.95E-63.

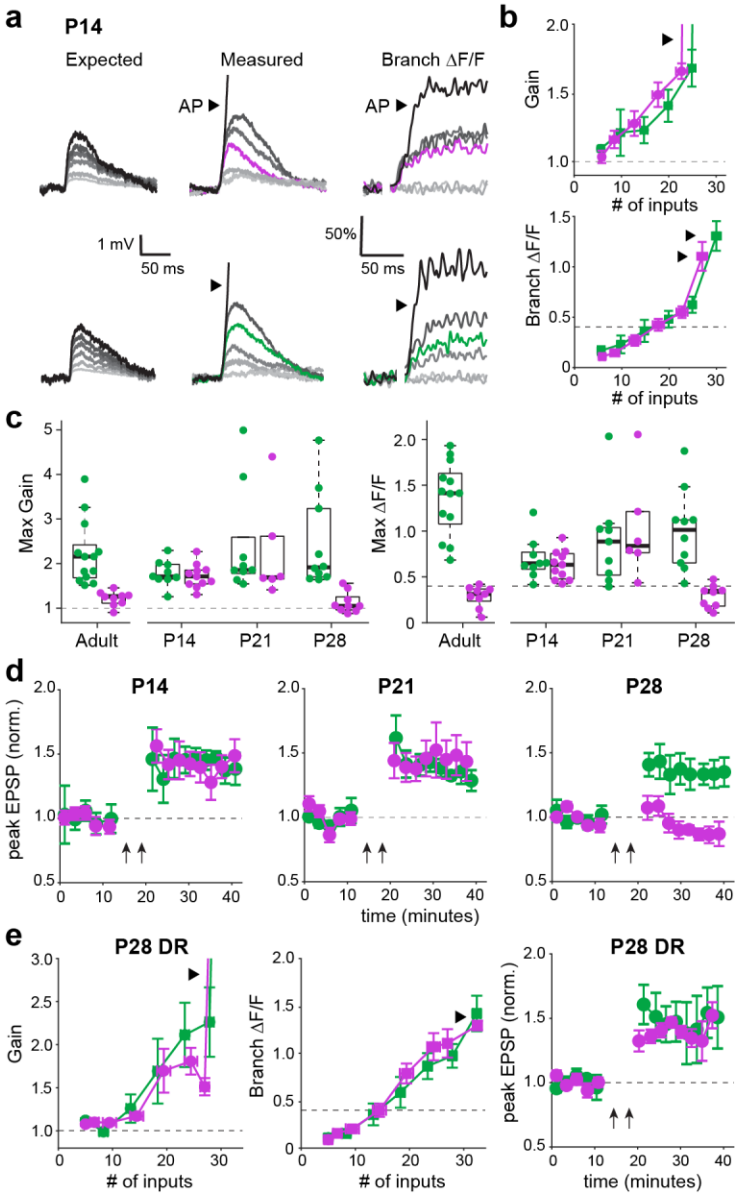

Figure 3: Developmental regulation of synaptic integration and plasticity in oblique versus basal dendrites.

a. Expected (left), measured (middle), and ΔF/F (right) for oblique (top) and basal (bottom) dendrites from the same neuron from a P14 mouse. Note supralinear integration and large Ca^{2+} signals in both branches. Both are driven to action potential (AP, arrow).
b. P14 population gain (measured/expected, left) and branch ΔF/F (right) (n = 9 basal branches and 9 oblique branches, both from 5 animals). Basal vs oblique gain*, p = 0.33; ΔF/F*, p = 0.70.
c. Maximum gain (left) and local branch ΔF/F (prior to AP initiation, right) across developmental time points (Adult, P56+: n as in Fig. 1, basal vs oblique gain*, p = 1.07E-04; ΔF/F*, p = 1.07E-04. P14: n as in b, basal vs oblique gain*, p = 0.54; ΔF/F*, p = 0.76. P21: n = 9 basal branches, 4 animals, 6 oblique branches, 2 animals, basal vs oblique gain*, p = 0.52; ΔF/F*, p = 0.68. P28: n = 10 basal branches, 5 animals; 9 oblique branches, 5 animals, basal vs oblique gain*, p = 2.17E-05; ΔF/F*: p = 4.33E-05.

d. Plasticity (as described in Fig. 2) in basal versus oblique dendrites at P14 (n = 5 basal branches from 5 animals and 5 oblique branches from 5 animals, basal vs oblique post-induction*, p = 0.79), P21 (n= 5 basal branches from 4 animals and 7 oblique branches from 6 animals, basal vs oblique post-induction*, p = 0.87), and P28 (n = 7 basal branches, 5 animals; 7 oblique branches, 4 animals, basal vs oblique post-induction*, p = 1.25E-13).
e. P28 population gain (measured/expected, left) and branch ΔF/F (middle) in dark-reared (DR) mice (n = 9 basal branches and 10 oblique branches from 4 animals, basal vs oblique gain*, p = 0.78; ΔF/F*, p = 0.96). Plasticity for dark-reared animals (right) (n = 5 apical branches from 4 animals and 6 oblique branches from 6 animals, basal vs oblique post-induction*, p = 0.81).

*Mann-Whitney U test was used for all comparisons.

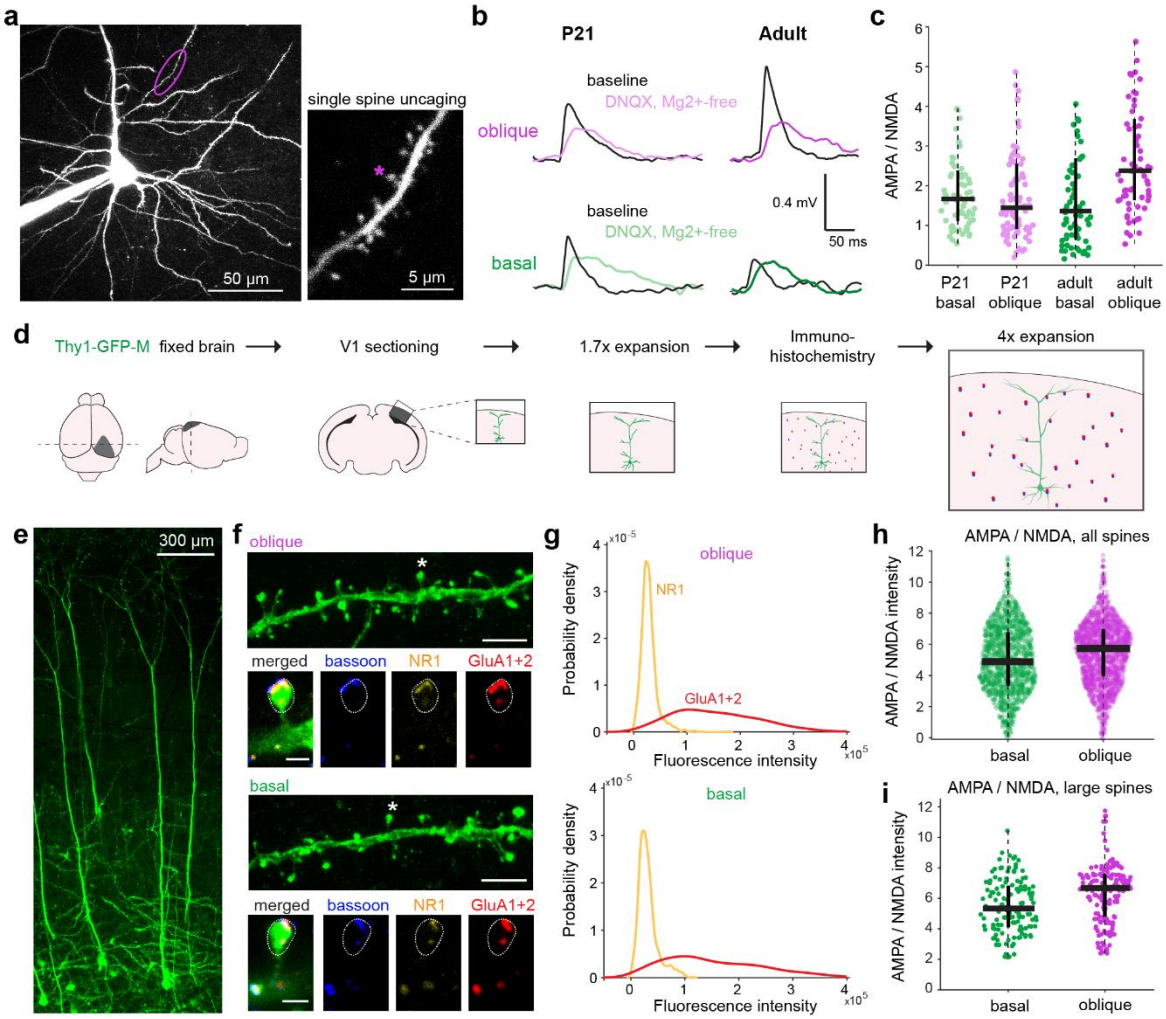

Figure 4: Changes in synaptic AMPA-to-NMDA ratio at oblique versus basal dendrites underlie differences in integration and plasticity.

a. Example two-photon image of a V1 L5 PN from a P21 mouse. An oblique dendrite (circled) is shown at higher magnification (right). Uncaging site indicated by star.
b. Representative average EPSPs from uncaging at single spines in P21 (left) or adult (right) mice from oblique (top) and basal (bottom) dendrites. Black traces: control, colored traces: the same spine in DNQX+Mg^{2+}-free ACSF.
c. Functional single spine AMPA/NMDA ratios from basal and oblique dendrites in P21 and adult mice (P21: n = 72 basal spines from 4 mice and 89 oblique spines from 4 mice. Adult, P56+: n = 66 basal spines from 4 mice and 67 oblique spines from 5 mice). Outliers are not shown. P21 basal vs oblique, Mann-Whitney U test: p = 0.23; adult basal vs oblique, Mann-Whitney U test: p = 1.00E-04.
d. Schematic of the epitope-preserving Magnified Analysis of the Proteome (eMAP) experimental procedure.
e. Confocal image of L5 PNs from a Thy1-GFP M P56+ mouse after 4x MAP expansion.
f. Example confocal images of expanded oblique (top) and basal (bottom) dendrites from the same neuron. For each branch, immunostaining for bassoon, NR1, and GluA1+2 is shown for one spine (indicated by star). Scale bar: 10 µm, spine inset: 2 µm.

g. Probability density of NR1 and GluA1+2 signals for all spines (n = 1,305 basal dendrite spines and 1,719 oblique dendrite spines from 13 cells, 3 mice).
h. Ratio of AMPA/NMDA intensities for all spines: Mann-Whitney U test: p = 8.30E-11.
i. Ratio of AMPA/NMDA intensities for the largest 10% of basal and oblique spines (n = 131 basal dendrite spines and 171 oblique dendrite spines). Mann-Whitney U test: p = 1.08E-04.